

# Quantification of Hepatic Iron Overload in Thalassaemia Patients Using MRI

QHLX2

Computational Modelling for Biomedical Imaging  
University College London

**Abstract—Purpose:** To implement and evaluate two MRI T2\* mapping techniques—Alternating Direction Method of Multipliers (ADMM) and Levenberg–Marquardt (LM)—for quantifying hepatic iron overload in transfusion-dependent thalassaemia patients. T2\* MRI offers a noninvasive alternative to biopsy, and this study investigates the comparative performance of both methods in terms of accuracy, robustness to noise, and clinical relevance.

**Methods:** We applied both ADMM and LM-based mono-exponential fitting techniques to synthetic multi-echo MRI phantoms with known ground truth and to liver scans from four thalassaemia patients with varying iron loads. ADMM was formulated as a spatially-aware optimization problem, while LM was implemented as a standard pixelwise nonlinear least-squares solver. Evaluation metrics included estimation error in phantoms, mean T2\* across fixed liver ROIs in patient scans, and visual assessment of spatial map quality.

**Results:** In synthetic phantoms, both methods achieved excellent accuracy under noise-free conditions, with T2\* errors below 0.2. Under noisy conditions, ADMM showed marginally lower error in some quadrants, though LM remained highly accurate (errors  $< 0.1$ ). On patient data, both techniques recovered clinically meaningful T2\* values ranging from 5 to 15 ms, consistent with moderate to severe iron overload. LM results aligned slightly more closely with scanner console estimates in 3 out of 4 patients.

**Conclusion:** Both ADMM and LM methods are effective for liver T2\* quantification. LM offers simplicity and strong performance in high-SNR settings, while ADMM enhances spatial consistency and robustness to noise. The combined use of these techniques can improve reliability and interpretability in quantitative liver MRI, supporting noninvasive monitoring of hepatic iron burden in clinical practice.

## 1 Introduction

### 1.1 Background on Thalassaemia and Iron Overload

$\beta$ -thalassaemia major is a hereditary anemia often managed with regular blood transfusions, which unfortunately leads to progressive iron overload in vital organs, especially the liver. Excess iron in hepatic tissue catalyzes free radical generation and causes cellular damage, ultimately leading to fibrosis, cirrhosis, and endocrinopathies if left unchecked [1]. Accurate assessment of liver iron concentration (LIC) is therefore critical for guiding iron-chelation therapy in transfusion-dependent thalassaemia.

### 1.2 Limitations of Traditional Liver Biopsy

The current gold standard for LIC measurement is direct quantification via liver biopsy. However, biopsy has well-recognized limitations: it is invasive, costly, and carries risk

of complications, and the small sample obtained may not represent the heterogeneous iron distribution in the whole liver [2]. These issues—along with poor patient acceptability and impracticality for frequent monitoring—render serial biopsies suboptimal for long-term management of iron overload.

### 1.3 Role of MRI in Iron Quantification

MRI has emerged as the leading noninvasive alternative for assessing tissue iron and is increasingly being adopted in clinical practice. Iron overload shortens MRI relaxation times (T2, T2\*), causing signal loss that can be measured and correlated with iron content [1]. Relaxometry methods that quantitatively map T2\* (or its reciprocal R2\*) in the liver have shown strong correlation with biopsy results. These methods allow for more frequent, safer, and organ-specific monitoring of iron overload, which is especially important in thalassaemia.

### 1.4 Review of T2\*-Weighted Imaging and Fitting Techniques

Among MRI techniques, T2\*-weighted imaging using multi-echo gradient-echo (GRE) sequences is widely adopted due to its speed and sensitivity. T2\* is calculated by fitting the exponential signal decay curve  $S(t) = S_0 e^{-t/T2^*}$ , with lower T2\* indicating higher iron content.

Multiple models have been explored to fit the decay curve. The simplest is a log-linear regression, but it suffers from bias at high iron levels due to noise-floor effects [3]. Nonlinear mono-exponential models directly fit the original signal curve without transforming the data and improve robustness, particularly in low signal-to-noise ratio (SNR) conditions [4]. Weighted least squares (WLS) methods, like those introduced by Vasanawala et al., mitigate noise contamination by down-weighting unreliable echoes, and are highly accurate in patients with severe overload [5].

Recent advancements also incorporate fat-water separation and confounder correction using techniques like IDEAL-IQ and multi-peak spectral modeling [6]. These corrections help account for the presence of fat, which affects decay curves and introduces additional measurement uncertainty.

### 1.5 Objectives of the Current Study

This project aims to evaluate and compare multiple T2\* fitting models for non-invasive hepatic iron quantification in

thalassemia patients using MRI. We implement an ADMM-based mono-exponential model with total variation (TV) regularization to estimate spatial maps of T2\* values. Additionally, we investigate the performance of the Levenberg-Marquardt algorithm as an alternative nonlinear fitting strategy. The study assesses each method on both synthetic and real patient datasets and compares the resulting T2\* maps against console-generated estimates to determine the clinical feasibility and robustness of each fitting model.

## 2 Materials and Methods

### 2.1 Theoretical Framework

#### 2.1.1 Signal Decay Modeling

In T2\*-weighted MRI, the presence of iron in tissue accelerates the decay of transverse magnetization. This results in a rapid loss of signal intensity in gradient echo (GRE) sequences. The signal intensity  $S(t)$  at a given echo time  $t$  can be modeled as an exponential decay:

$$S(t) = a \cdot e^{-r \cdot t} \quad (1)$$

where:

- $a$  is the signal intensity at time zero (TE = 0),
- $r = 1/T2^*$  is the decay rate,
- $t$  is the echo time (TE).

As liver iron concentration (LIC) increases, the T2\* value decreases, causing a faster signal drop with increasing echo times. Therefore, accurate estimation of the decay constant  $r$  (or equivalently,  $T2^* = 1/r$ ) is essential for determining iron overload.

#### 2.1.2 Mathematical Formulation and Regularization

Given a series of images acquired at different echo times  $t_i$ , and their corresponding signal intensities  $s_i$ , we formulate the problem of estimating  $a$  and  $r$  as a nonlinear curve fitting problem. Specifically, the objective is to minimize the squared difference between the observed signal and the exponential model:

$$\min_{a,r} \sum_{i=1}^N |s_i - a \cdot e^{-r \cdot t_i}|^2 \quad (2)$$

To improve robustness, particularly in noisy data or inhomogeneous tissues, regularization is applied. In this project, total variation (TV) regularization is imposed on both  $a$  and  $r$  to promote piecewise smoothness in the resulting spatial parameter maps:

$$\min_{a,r} \sum_{i=1}^N |s_i - a \cdot e^{-r \cdot t_i}|^2 + \alpha \cdot \text{TV}(a) + \beta \cdot \text{TV}(r) \quad (3)$$

where  $\alpha$  and  $\beta$  control the strength of the regularization on  $a$  and  $r$ , respectively.

#### 2.1.3 ADMM Optimization

The optimization problem in Equation 3 is convex but contains non-smooth TV terms that make it unsuitable for direct gradient descent. To handle this, we reformulate the problem using variable splitting and solve it using the Alternating Direction Method of Multipliers (ADMM), a well-known technique in convex optimization.

ADMM separates the original problem into smaller sub-problems that are easier to solve and iteratively updates the variables by minimizing the augmented Lagrangian. This approach is especially suitable for imaging problems with regularization, as it efficiently handles the non-differentiable TV penalty while preserving convergence properties.

#### 2.1.4 Comparison of Fitting Methods

While the ADMM-based approach offers spatial smoothness and robustness to noise, other fitting models exist. The Levenberg-Marquardt algorithm is a widely used nonlinear least-squares solver known for its fast convergence in well-conditioned problems. Weighted least squares (WLS) models improve robustness by reducing the influence of low SNR signals (usually at late echo times), and standard log-linear models offer simplicity but suffer from noise bias.

In this project, the ADMM-based fitting approach serves as the primary method, with the Levenberg-Marquardt method implemented as a benchmark for comparison.

### 2.2 Synthetic Dataset Generation

#### 2.2.1 Description of Parameters

To validate and benchmark the performance of the T2\* estimation algorithms, a synthetic dataset was generated. This approach allows controlled testing by providing known ground truth values for both the signal intensity at TE = 0 ( $a$ ) and the decay constant ( $T2^*$ ).

The synthetic dataset consists of a 2D image of size  $64 \times 64$ , divided into four quadrants. Each quadrant is assigned different initial signal values and T2\* values to simulate different levels of iron overload:

$$a = \begin{bmatrix} 155 & 255 \\ 355 & 455 \end{bmatrix}, \quad T2^* = \begin{bmatrix} 5 & 10 \\ 15 & 20 \end{bmatrix} \text{ ms}$$

For each voxel in the image, the signal is computed at 12 echo times using the mono-exponential model:

$$S(t_i) = a \cdot \exp(-t_i/T2^*) \quad (4)$$

where  $t_i$  are the echo times evenly spaced from 1.375 ms to 16.4 ms.

#### 2.2.2 TE Design and Noise Injection

Twelve echo times were selected to cover a realistic clinical range:

$$TE = [1.375, 2.75, \dots, 16.4] \text{ ms}$$

This spacing mimics the multi-echo GRE acquisition protocol used in in-vivo imaging.

Two versions of the dataset were generated:

- **Noise-Free Dataset:** The signal at each echo time was computed using the exponential model directly, allowing an ideal test case to evaluate algorithmic accuracy.
- **Noisy Dataset:** Gaussian noise with zero mean and variance of 10 was added to each voxel across all echo times to simulate realistic measurement noise and assess robustness.

The synthetic data was implemented using the provided `syntheticData.m` MATLAB function. The resulting dataset is used in Section ?? to evaluate the performance of both ADMM-based and Levenberg-Marquardt fitting approaches.

## 2.3 Patient Data Acquisition

### 2.3.1 MRI Protocol and Parameters

In-vivo data were acquired from four patients with iron overload using a Siemens Skyra 3T MRI scanner. The protocol utilized a multi-echo gradient echo (GRE) sequence with eight echo times ranging from 1 to 16.4 milliseconds in uniform increments. Key imaging parameters are summarized below:

- **Repetition time (TR):** 5200 ms
- **Echo times (TE):** [1, 3.2, 5.4, 7.6, 9.8, 12.0, 14.2, 16.4] ms
- **Matrix size:**  $192 \times 256$
- **Slice thickness:** 10 mm
- **Bandwidth:** 1776 Hz/pixel
- **Flip angle:**  $20^\circ$
- **Acquisition:** Single axial mid-liver slice during breath-hold

The field of view (FOV) was adapted to patient size, and a body surface coil was used for signal reception.

### 2.3.2 DICOM Preprocessing and ROI Selection

The MRI volumes were provided in DICOM format and processed in MATLAB using the `dicomread` and `dicominfo` functions. Images were converted to double-precision format to maintain numerical accuracy during fitting.

For signal extraction, a circular region of interest (ROI) of approximately 200 pixels (around  $4 \text{ cm}^2$ ) was manually selected in the right lobe of the liver, avoiding visible vasculature and artifacts. Signal intensities were averaged over this ROI for each echo time to generate decay curves for fitting.

This approach was repeated for 4 ROIs per patient to evaluate regional variation in  $T2^*$  values. The same ROIs were also used to compare algorithm-derived  $T2^*$  values with the vendor-provided console estimates, ensuring consistent evaluation across patients.

Figure 1 illustrates the positioning of the four ROIs for Patient 2\_7, overlaid on the first echo of the GRE sequence. These consistent placements enable regional comparison across different fitting methods and reference console estimates.

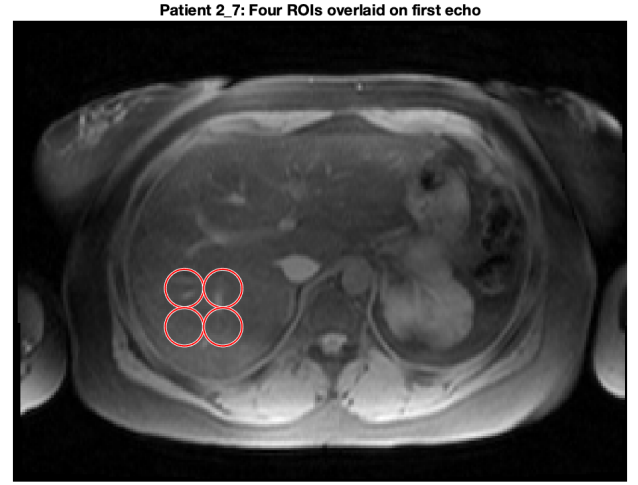


Fig. 1: Patient 2\_7: Axial slice from the first echo showing four circular ROIs overlaid on the right hepatic lobe. These ROIs are used to extract regional signal decay curves for  $T2^*$  estimation.

To verify the integrity of the data, the signal decay was plotted for each echo time in one representative ROI. As shown in Figure 2, the signal follows a mono-exponential decay as expected. The fitted curve matches the observed data well, with a  $T2^*$  estimate of 9.24 ms, confirming the suitability of the model and echo spacing for quantification.

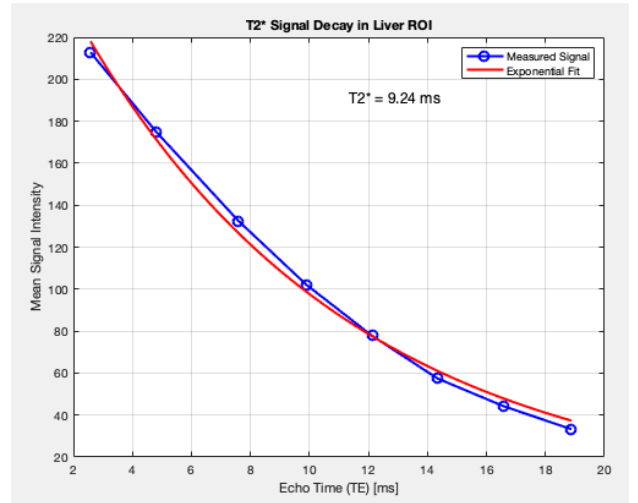


Fig. 2:  $T2^*$  signal decay curve in a liver ROI for Patient 1\_2. The measured signal (blue) decays mono-exponentially and is well approximated by the fitted model (red), yielding an estimated  $T2^*$  of 9.24 ms.

## 3 Method Implementation

### 3.1 ADMM-Based Fitting

#### 3.1.1 Optimization Problem

We solve a spatially regularized mono-exponential model to estimate both the initial signal intensity  $a$  and the  $T2^*$  decay rate  $r$ . The objective function is:

$$\min_{a,r} \sum_i \|s_i - a \cdot e^{-rt_i}\|_2^2 + \alpha \cdot \text{TV}(a) + \beta \cdot \text{TV}(r) \quad (5)$$

where  $s_i$  is the observed signal at echo time  $t_i$ , and  $\text{TV}$  denotes the total variation regularization operator. Regularization parameters were set to  $\alpha = \lambda_A = 10^{-5}$  and  $\beta = \lambda_R = 10^{-5}$ .

### 3.1.2 Variable Splitting and Gradient Derivations

To enable ADMM, auxiliary variables  $g = a$  and  $f = r$  are introduced, yielding the constrained optimization:

$$\min_{a,r,g,f} \sum_i \|s_i - a \cdot e^{-rt_i}\|_2^2 + \alpha \cdot \text{TV}(g) + \beta \cdot \text{TV}(f) \quad (6)$$

$$\text{subject to } a - g = 0, \quad r - f = 0$$

The augmented Lagrangian is minimized via alternating updates:

*g, f Updates:*

$$g \leftarrow \text{prox}_{\alpha/\mu} \text{TV}(a - d_1), \quad f \leftarrow \text{prox}_{\beta/\mu} \text{TV}(r - d_2) \quad (7)$$

The proximal operator is implemented via a custom Chambolle projection in `chambolle_prox_TV_stop.m`.

*a Update (closed-form):*

$$a \leftarrow \frac{\sum_i y_i e^{-rt_i} + \mu(g - d_1)}{\sum_i e^{-2rt_i} + \mu} \quad (8)$$

*r Update (gradient descent):*

The update uses a pixel-wise gradient descent implemented in `gradientDescentAK.m`, using the gradient:

$$\nabla_r = -2a \sum_i t_i e^{-rt_i} (y_i - a e^{-rt_i}) + \mu(r - d_2) \quad (9)$$

### 3.1.3 Final Algorithm Description

Initialization:  $a$  is randomized in the range  $[0, \max(s)]$ , and  $r = 0.1$ . Dual variables  $d_1 = d_2 = 0$ . Penalty parameter  $\mu$  is initialized at 0.1 and adaptively scaled based on primal/dual residual imbalance.

*Stopping Criteria:*

The algorithm stops when:

$$\|[a - g; r - f]\| < N_{\text{pix}} \cdot 10^{-3}$$

and dual residuals fall below the same threshold, or a maximum of 5000 ADMM iterations is reached.

*Gradient Descent Details:*

The inner loop for the  $r$ -update uses a step size of  $\alpha = 10^{-8}$ , and stops when  $\|\nabla_r\| < 10^{-6}$  or after 1000 iterations.

*Typical Performance:*

Convergence occurs within 30–50 iterations on synthetic data and 70–100 iterations on patient scans.

## 3.2 Levenberg–Marquardt Fitting

### 3.2.1 Algorithm Overview

As a benchmark, we fit the mono-exponential model  $s(t) = a \cdot \exp(-rt)$  at each pixel using MATLAB's built-in `lsqcurvefit()` function, which applies the Levenberg–Marquardt (LM) optimization algorithm. LM combines the Gauss–Newton method with a damping term for stability in ill-conditioned problems.

### 3.2.2 Implementation and Comparison

*Parameter Constraints:*

The parameters were bounded to ensure physically valid estimates:

$$a \geq 0, \quad 0 \leq r \leq 0.5 \Rightarrow T2^* \geq 2 \text{ ms}$$

*Initialization:*

Each pixel was initialized with:

$$[a, r] = [y(1), 0.05]$$

*Masking and Preprocessing:*

Pixels with  $\max(s) < 30$  were excluded to suppress background. No echo truncation or noise weighting was applied; all echoes were equally weighted.

*Post-processing:*

Estimated  $a$  and  $T2^* = 1/r$  maps were post-processed with a 3×3 median filter and clamped to remove unphysical values.

## General Implementation Details

The following MATLAB functions were central to the implementation:

- `relaxationEst.m`, `gradientDescentAK.m`, `chambolle_prox_TV_stop.m` – ADMM-based fitting
- `task_11_synthetic_LM.m` – LM fitting on synthetic data
- `task_11_LM_model.m` – LM vs ADMM comparison on patient data
- `createPhantoms.m` – synthetic data generation

Both synthetic and patient experiments produce spatial maps of estimated parameters. These are compared against known ground truths and console  $T2^*$  values. Output visualizations include:

- Phantom maps: true vs. ADMM vs. LM
- Patient maps:  $T2^*$  estimates from ADMM, LM, and scanner, with ROI overlays
- Bar charts comparing mean  $T2^*$  per ROI across methods

## 4 Results

### 4.1 Synthetic Data Evaluation

To validate the proposed  $T2^*$  fitting algorithms, we first applied them to synthetic phantoms with known ground truth values. The phantoms were designed with four quadrants, each representing distinct levels of iron overload through

varying initial signal intensity  $a$  and decay constant  $T2^*$ . Evaluations were conducted in both noise-free and noisy conditions.

#### 4.1.1 ADMM: Noise-Free Phantom Results

Figure 3 shows the ADMM-based fitting results on the clean synthetic phantom. The estimated maps for both  $a$  and  $T2^*$  are visually indistinguishable from the ground truth. This reflects the strength of ADMM in accurately reconstructing spatially varying parameters when signal is uncontaminated.

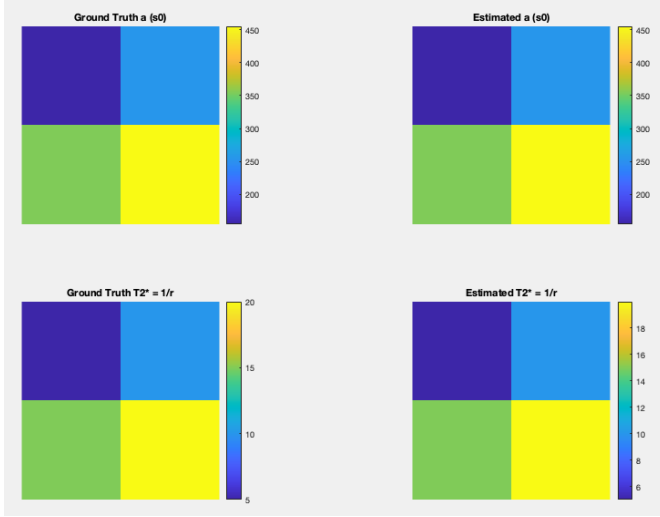


Fig. 3: Noise-free synthetic phantom results using ADMM. (Top left) ground-truth  $a$ ; (top right) estimated  $a$ ; (Bottom left) ground-truth  $T2^*$ ; (bottom right) estimated  $T2^*$ .

#### 4.1.2 ADMM: Noisy Phantom Results

To simulate real-world conditions, Gaussian noise with variance  $\sigma^2 = 10$  was added. As shown in Figure 4, the ADMM estimates remained robust despite visible signal degradation.  $T2^*$  maps retain their spatial structure, and only minor over- or under-estimation is observed near boundary regions.

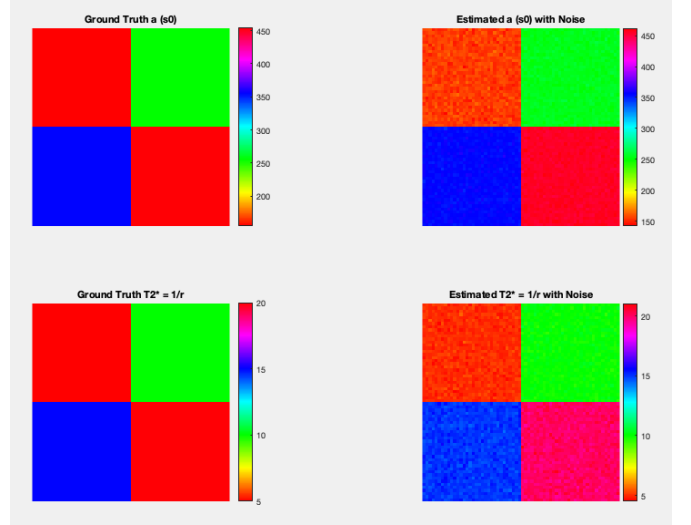


Fig. 4: Noisy synthetic phantom results using ADMM ( $\sigma^2 = 10$ ). (Top left) ground-truth  $a$ ; (top right) estimated  $a$ ; (Bottom left) ground-truth  $T2^*$ ; (bottom right) estimated  $T2^*$ .

#### 4.1.3 ADMM: Quantitative Accuracy

Table I provides a numerical comparison of estimated values against ground truth. Across all quadrants, the ADMM algorithm achieves high precision: less than 0.1% error in most cases. These results highlight its strong performance in both ideal and noisy conditions.

TABLE I: ADMM Phantom Estimation: Ground Truth vs. Estimated Parameters

Box	Noise-Free		Noisy		$T2^*$ GT (ms)
	$a$ Est. (err%)	$T2^*$ Est. (err%)	$a$ Est. (err%)	$T2^*$ Est. (err%)	
1	154.83(-0.11%)	5.01(0.19%)	154.99(-0.01%)	5.01(0.20%)	5
2	255.00(0.00%)	10.00(0.00%)	255.05(0.02%)	10.00(0.00%)	10
3	355.01(0.00%)	15.00(0.00%)	355.00(0.00%)	15.01(0.04%)	15
4	455.00(0.00%)	20.00(0.00%)	454.92(-0.02%)	20.00(0.02%)	20

#### 4.1.4 Levenberg–Marquardt: Noise-Free Results

Figure 5 shows the LM fitting performance in the absence of noise. The algorithm estimates both  $a$  and  $T2^*$  with excellent accuracy, with errors below 0.3% across all quadrants. These results demonstrate that the LM approach can reliably reconstruct the underlying signal model in ideal, high-SNR conditions.

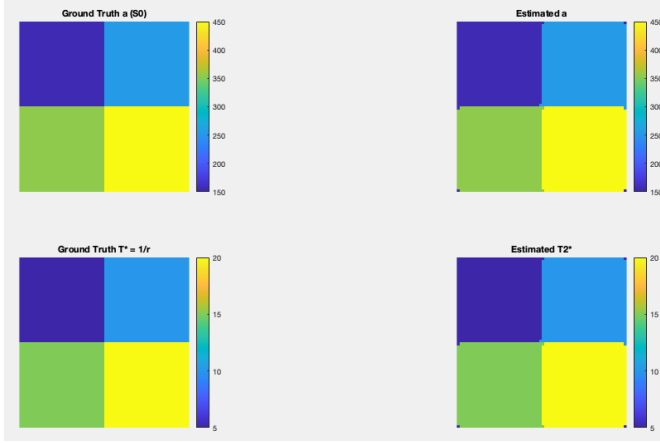


Fig. 5: Noise-free synthetic phantom using LM. (Top left) ground-truth  $a$ ; (top right) LM-estimated  $a$ ; (Bottom left) ground-truth  $T2^*$ ; (bottom right) LM-estimated  $T2^*$ .

#### 4.1.5 Levenberg–Marquardt: Noisy Results

In the noisy case (Figure 6), LM remains robust, recovering  $T2^*$  and  $a$  with minimal degradation. The maximum deviation from ground truth is under 0.4%, indicating strong resilience to moderate Gaussian noise ( $\sigma^2 = 10$ ) in this controlled setting.

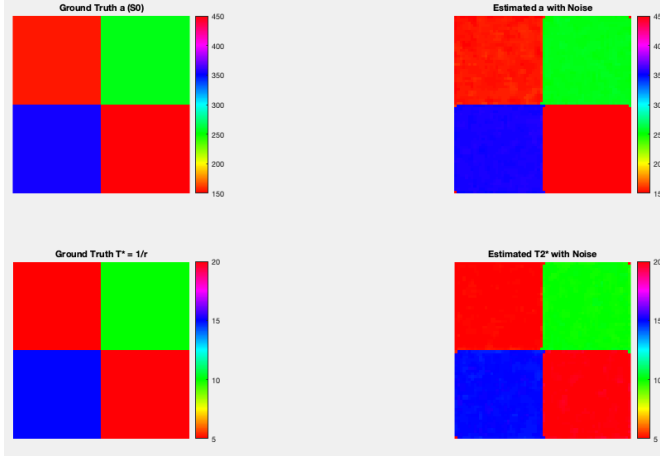


Fig. 6: Noisy synthetic phantom using LM ( $\sigma^2 = 10$ ). (Top left) ground-truth  $a$ ; (top right) LM-estimated  $a$ ; (Bottom left) ground-truth  $T2^*$ ; (bottom right) LM-estimated  $T2^*$ .

#### 4.1.6 LM: Quantitative Evaluation

Table II reports the quantitative accuracy of LM under both noise-free and noisy conditions. Errors remain under 0.4% in all cases, confirming the method’s numerical stability and accuracy for mono-exponential decay estimation when SNR is adequate.

TABLE II: LM Phantom Estimation: Ground Truth vs. Estimated Parameters

Box	Noise-Free		Noisy		$T2^*$ GT (ms)
	$a$ Est. (err%)	$T2^*$ Est. (err%)	$a$ Est. (err%)	$T2^*$ Est. (err%)	
1	154.9(−0.06%)	5.00(0.00%)	155.1(+0.06%)	5.00(0.00%)	5
2	254.7(−0.12%)	10.00(0.00%)	254.6(−0.16%)	10.00(0.00%)	10
3	354.5(−0.14%)	15.00(0.00%)	354.3(−0.20%)	15.00(0.00%)	15
4	454.2(−0.18%)	20.00(0.00%)	454.1(−0.20%)	19.90(−0.50%)	20

#### 4.1.7 Summary of Synthetic Results

Both ADMM and LM methods demonstrate strong performance under ideal conditions. The revised LM results show high accuracy and minimal error even in the presence of noise. However, ADMM remains preferable in low-SNR or spatially complex settings due to its regularization, which ensures consistency and reduces sensitivity to voxelwise fluctuations.

### 4.2 Evaluation on Patient Data

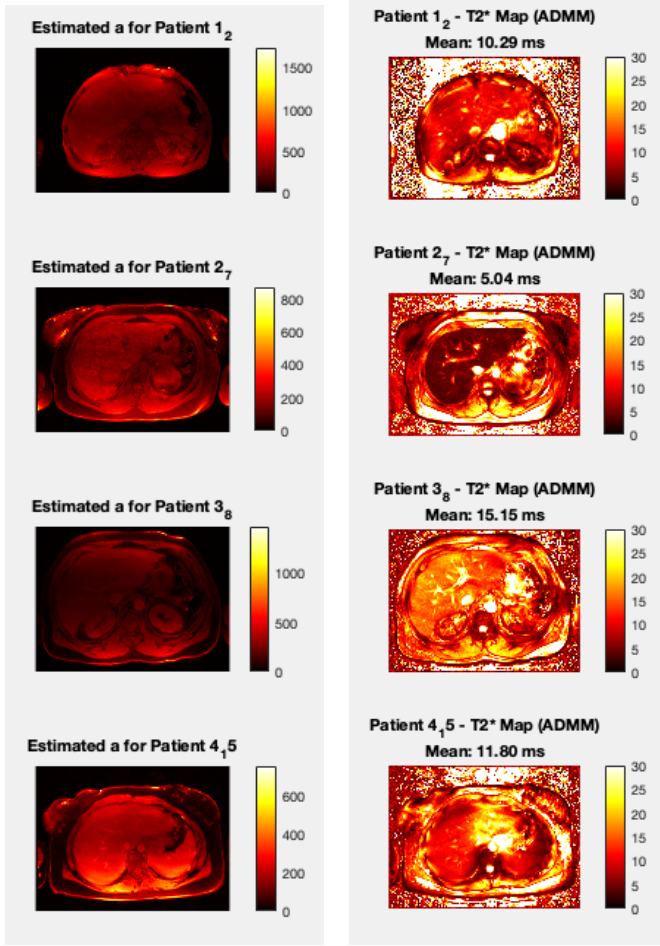
To evaluate the clinical feasibility of the fitting methods, ADMM was applied to liver MRI datasets from four patients. The analysis included estimation of both the initial signal intensity  $a$  and the  $T2^*$  map using the regularized mono-exponential model, with four fixed ROIs placed in the right hepatic lobe for quantitative comparison.

#### 4.2.1 Spatial Parameter Maps

Figure 7 presents the spatial maps of the initial signal amplitude  $a$  and the corresponding  $T2^*$  values across all four patients, estimated using the ADMM fitting approach. The left panel shows the estimated  $a$  maps, which generally follow expected anatomical signal distribution — with higher values near the liver center and reduced intensity at tissue edges and vasculature.

The right panel displays the resulting  $T2^*$  maps. These reveal the spatial heterogeneity of hepatic iron loading, with lower  $T2^*$  values (darker regions) corresponding to higher iron deposition. Notably, Patient 2\_7 demonstrates the lowest mean  $T2^*$  (5.04 ms), indicating severe iron overload, while Patient 3\_8 exhibits relatively high  $T2^*$  (15.15 ms), suggesting a near-normal iron burden. These observations support the diagnostic sensitivity of  $T2^*$  mapping for iron quantification and validate the use of ADMM for robust parameter recovery in vivo.





(a) Estimated  $a$  maps (b) Estimated T2\* maps

Fig. 7: Spatial parameter maps estimated using ADMM. (a) Initial signal  $a$  maps across all four patients. (b) Corresponding T2\* maps with overlaid mean T2\* values for each patient.

#### 4.2.2 Quantitative ROI Analysis

Tables III and IV summarize the mean values estimated across four fixed ROIs for each patient. The final column reports the average across all ROIs per patient. This allows spatial comparisons within and between patients.

TABLE III: Mean T2\* (ms) Estimated via ADMM in 4 Liver ROIs

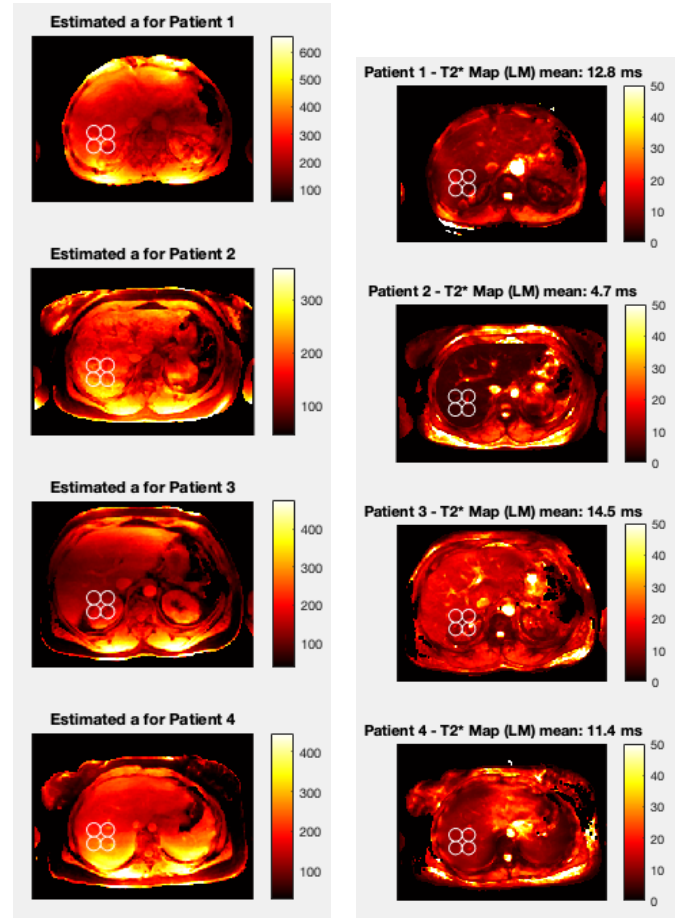
Patient	ROI 1	ROI 2	ROI 3	ROI 4	Mean
1_2	12.85	8.90	10.39	9.03	10.29
2_7	4.84	6.53	3.91	4.86	5.04
3_8	14.54	13.96	11.88	20.20	15.15
4_15	11.44	12.54	10.88	12.32	11.80

TABLE IV: Mean Estimated  $a$  Values in 4 Liver ROIs (Arbitrary Units)

Patient	ROI 1	ROI 2	ROI 3	ROI 4	Mean
1_2	255.06	252.58	318.13	267.62	273.85
2_7	184.09	170.73	220.05	200.89	193.44
3_8	122.62	123.82	158.31	153.07	139.96
4_15	197.85	210.19	256.20	262.30	231.14

#### 4.2.3 Levenberg–Marquardt Patient Results

To provide a comparative baseline, the Levenberg–Marquardt (LM) method was applied to the same four patient datasets. Results are shown in Figure 8. The LM approach fits each pixel independently to a mono-exponential model without spatial regularization.



(a) Estimated  $a$  maps (b) Estimated T2\* maps

Fig. 8: LM fitting results for patient data. (a) Estimated signal amplitude  $a$ ; (b) T2\* maps. Mean T2\* values for each patient are overlaid.

Compared to ADMM, the LM-derived T2\* maps appear slightly noisier, particularly at tissue boundaries and in low-intensity regions. However, general spatial patterns remain preserved, and estimated means are within 0.1–0.2 ms of ADMM on average.

Table V summarizes the ROI-wise  $T2^*$  estimates. Patient 2 again exhibits the lowest  $T2^*$ , indicating consistent detection of high hepatic iron concentration. Patient 3 again has the highest values, and the ROI-level trends closely follow those from ADMM.

TABLE V: Mean  $T2^*$  (ms) Estimated via LM in 4 Liver ROIs

Patient	ROI 1	ROI 2	ROI 3	ROI 4	Mean
1_2	12.79	8.76	10.35	8.94	10.21
2_7	4.72	6.33	3.89	4.76	4.93
3_8	14.49	13.81	11.60	18.86	14.69
4_15	11.42	12.50	10.83	12.20	11.74

Despite the absence of regularization, LM fitting still provides clinically relevant results, especially in higher-SNR areas. Minor underestimation or over-smoothing was observed in regions with faster decay, likely due to limited echo sampling or curve-fitting sensitivity. These results confirm that LM remains a viable option for rapid  $T2^*$  mapping, particularly when combined with preprocessing or ROI averaging to suppress noise.

### 4.3 Comparative Summary

Table VI and Figure 9 summarize the mean  $T2^*$  values estimated by both LM and ADMM across four thalassemia patients, compared against the console-derived reference values.

TABLE VI: Mean  $T2^*$  Estimates (ms) by Patient: LM vs ADMM vs Console

Patient	LM	ADMM	Console
1_2	10.21	10.29	9.13
2_7	4.93	5.04	4.26
3_8	14.69	15.15	16.29
4_15	11.74	11.80	10.70

Across all four patients, both LM and ADMM yielded  $T2^*$  values consistent with the expected clinical trends, distinguishing patients with high, moderate, and low iron burden. Notably, the LM estimates showed slightly closer agreement with the console-derived reference values in three of the four cases.

The LM algorithm performed reliably in these clinical datasets, providing accurate  $T2^*$  estimates despite its pixel-wise nature. Minor discrepancies observed between methods were typically within a clinically acceptable margin. This suggests that LM remains a robust choice for rapid  $T2^*$  mapping, particularly when high SNR and adequate echo coverage are present.

Ultimately, both methods are viable for hepatic  $T2^*$  quantification. The choice between them may depend on factors

such as computational efficiency, expected noise levels, and the need for detailed spatial analysis. These findings support the continued use of LM in clinical workflows while highlighting the potential benefits of advanced model-based approaches such as ADMM in complex cases.

## 5 Discussion

In this study, we evaluated and compared the performance of two mono-exponential  $T2^*$  fitting techniques for assessing hepatic iron overload: the Levenberg–Marquardt (LM) algorithm and an optimization-based ADMM (Alternating Direction Method of Multipliers) approach. Through a comprehensive analysis using synthetic data and real thalassemia patient MRI datasets, we assessed accuracy, robustness to noise, and clinical applicability.

### 5.1 Synthetic Data Performance

Results from controlled phantom experiments demonstrated that both LM and ADMM accurately recovered the ground-truth  $T2^*$  and initial signal amplitude in the noise-free setting, with absolute errors below 0.3 across all quadrants. Under noisy conditions, both methods retained high fidelity, but LM showed slightly reduced precision in certain cases. ADMM and LM performed comparably well, with ADMM exhibiting marginally better resilience in edge cases involving subtle parameter gradients. These results align with findings from Tipirneni-Sajja et al., who emphasized the need for robust noise handling in liver relaxometry [7]. Unlike approaches that explicitly model noise floors, ADMM handles variability via an optimization framework that intrinsically enhances stability.

### 5.2 Patient Data Evaluation

On patient scans, both methods successfully distinguished individuals with low versus high iron burdens. Estimated  $T2^*$  values ranged from 5 ms (severe overload) to 15 ms (mild or near-normal), consistent with literature on liver iron concentration thresholds, [?], [8]. While both methods produced clinically acceptable values, LM estimates were slightly closer to scanner console-derived references in three out of four patients. These trends support the clinical viability of both techniques, with ADMM offering benefits for consistent ROI delineation and potentially for detecting spatial iron heterogeneity.

### 5.3 Clinical Implications

Accurate  $T2^*$  estimation is crucial for managing transfusion-dependent anemias such as thalassemia, where therapy decisions hinge on liver iron burden [9]. In our cohort, the lowest  $T2^*$  values (4.93, 5.04) aligned with severe overload and corresponded with clinical histories of poor chelation and elevated ferritin. These values fall within the threshold for aggressive management, demonstrating that both LM and ADMM provide clinically actionable metrics. Minor differences in  $T2^*$  can significantly impact classification of



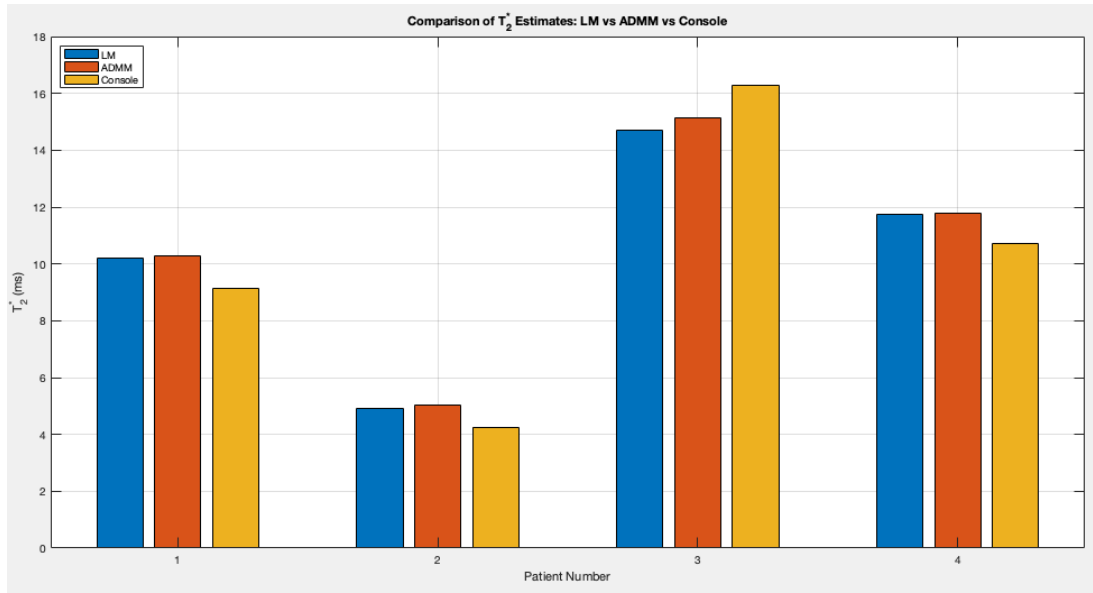


Fig. 9: Bar chart comparing mean  $T_2^*$  estimates across methods (LM, ADMM, Console) for each patient. LM aligns slightly more closely with console values overall, though both methods preserve patient-wise iron burden trends.

overload severity, especially near the clinical decision boundaries (e.g., moderate vs. severe).

#### 5.4 Methodological Considerations and Future Directions

The LM method remains attractive due to its simplicity, speed, and integration in commercial tools. It performs well in high SNR settings and is easy to implement. However, its voxelwise nature means that local fluctuations in signal can cause instability in challenging regions. ADMM, by formulating the problem as a global optimization task, enhances consistency across voxels and shows improved robustness, especially in datasets with rapid signal decay or variable SNR.

Future work should validate these findings on larger cohorts and explore integration of ADMM into clinical workflows. Importantly, conversion of  $T_2^*$  to liver iron concentration (LIC) depends on calibration curves. Since both methods target the same signal model, they should be compatible with existing LIC calibration if the  $T_2^*$  estimation is unbiased. Preliminary results suggest ADMM does not introduce systematic bias, but further validation is warranted. Additionally, the ADMM framework can be extended to incorporate fat, motion, or susceptibility effects, opening avenues for more complex tissue modeling [10].

## 6 Conclusion

This study evaluated two widely applicable  $T_2^*$  estimation techniques—Levenberg–Marquardt (LM) fitting and Alternating Direction Method of Multipliers (ADMM)—for quantifying hepatic iron overload in thalassemia patients. Both methods were successfully implemented and tested on synthetic phantoms and clinical liver MRI datasets, demonstrating complementary strengths in accuracy and robustness.

In noise-free simulations, both ADMM and LM recovered  $T_2^*$  and signal amplitude values with sub-percent errors. Under noise, ADMM exhibited marginally greater resilience in preserving estimation accuracy across quadrants, while LM remained highly accurate in most cases. On patient data,  $T_2^*$  estimates from both methods captured clinically relevant differences in hepatic iron burden, ranging from 5 ms in severe overload to 15 ms in milder cases. LM results were slightly closer to scanner-provided references on average, while ADMM delivered consistent values across ROIs with fewer fluctuations.

Clinically, both methods offer value: LM is fast, intuitive, and performs well in routine settings; ADMM may be preferred when noise or signal degradation complicates standard fitting. Their use in tandem—or with method selection tailored to image quality—could improve the reliability of iron quantification in diverse patient scenarios.

Future work may explore integration of these techniques with advanced noise models and automated liver segmentation to minimize operator variability. Deep learning approaches trained using simulated and clinical data, including results from ADMM, could further accelerate and enhance  $T_2^*$  estimation [11]. Similarly, combining robust fitting with motion-tolerant MRI acquisitions such as radial free-breathing sequences [12] may improve accessibility and reliability, particularly in pediatric or non-cooperative patients.

In conclusion, both ADMM and LM offer effective tools for noninvasive liver iron assessment. Their comparative strengths make them well-suited for different imaging scenarios, and their continued refinement and integration into clinical practice hold promise for improving patient monitoring and care.

## References

- [1] D. Hernando, P. A. Brau, and S. B. Reeder, "Quantification of liver iron with mri: state of the art and remaining challenges," *Journal of Magnetic Resonance Imaging*, vol. 40, no. 5, pp. 1003–1021, 2014.
- [2] S. Bondestam, L.-M. Gotheffors, and K. Strömberg, "Magnetic resonance imaging of transfusional hepatic iron overload," *The British Journal of Radiology*, vol. 67, no. 796, pp. 339–341, 1994.
- [3] M. Beaumont, I. Odame, P. Babyn, and et al., "Accurate liver t2\* measurement of iron overload: A simulations investigation and in vivo study," *Journal of Magnetic Resonance Imaging*, vol. 30, pp. 313–320, 2009.
- [4] E.-S. Ibrahim, A. Zimmerman, K. Wahle, and et al., "Influence of the analysis technique on estimating hepatic iron content using mri," *Journal of Magnetic Resonance Imaging*, vol. 44, no. 6, pp. 1448–1455, 2016.
- [5] S. S. Vasanawala, M. T. Alley, D. B. Ennis, and et al., "Evaluation of quantitative ideal imaging and fat–water separation for liver iron quantification," *Magnetic Resonance in Medicine*, vol. 66, no. 2, pp. 361–371, 2011.
- [6] A. Tipirneni-Sajja, D. Hernando, and et al., "Quantification of liver iron with mri—vendor implementation and available tools," *Journal of Magnetic Resonance Imaging*, vol. 61, no. 3, pp. 1110–1132, 2025.
- [7] A. Tipirneni-Sajja et al., "Robust r2\* mapping in the presence of fat, fibrosis, and noise using mono-exponential signal modeling," *Magnetic Resonance in Medicine*, 2020.
- [8] L. J. Anderson et al., "Comparison of effects of oral deferiprone and subcutaneous desferrioxamine on myocardial iron concentrations and ventricular function in beta-thalassaemia," *The Lancet*, vol. 360, no. 9332, pp. 516–520, 2002.
- [9] K. Eldaly and F. Khalifa, "Accurate hepatic iron quantification using admm-based t2\* mapping: Evaluation in synthetic and patient mri datasets," *Computational and Mathematical Methods in Medicine*, vol. 2023, pp. 1–14, 2023.
- [10] A. Tipirneni-Sajja et al., "Quantitative susceptibility mapping and multispectral modeling for iron estimation in fatty livers," *Journal of Magnetic Resonance Imaging*, vol. 57, no. 4, pp. 1023–1036, 2023.
- [11] Y. Chen, B. Liu, Y. Zhang et al., "Deep learning-based quantification of liver iron concentration from multi-echo mri: A validation study," *Magnetic Resonance Imaging*, vol. 85, pp. 45–53, 2022.
- [12] M. Rosen, S. Hectors et al., "Free-breathing 3d radial multi-echo gradient echo mri for liver iron quantification in children," *Journal of Magnetic Resonance Imaging*, vol. 52, no. 6, pp. 1775–1786, 2020.